# Carbon aerogels prepared by autocondensation of flavonoid tannin

A. Szczurek, V. Fierro, G. Medjahdi, A. Celzard

▶ **To cite this version:**

A. Szczurek, V. Fierro, G. Medjahdi, A. Celzard. Carbon aerogels prepared by autocondensation of flavonoid tannin. Carbon Resources Conversion, 2019, 2 (1), pp.72-84. 10.1016/j.crcon.2019.02.001 . hal-02357780

**HAL Id: hal-02357780**
**https://hal.science/hal-02357780**

Submitted on 19 Dec 2020

**HAL** is a multi-disciplinary open access archive for the deposit and dissemination of scientific research documents, whether they are published or not. The documents may come from teaching and research institutions in France or abroad, or from public or private research centers.

L'archive ouverte pluridisciplinaire **HAL**, est destinée au dépôt et à la diffusion de documents scientifiques de niveau recherche, publiés ou non, émanant des établissements d'enseignement et de recherche français ou étrangers, des laboratoires publics ou privés.

Carbon Resources Conversion 2 (2019) 72–84

Contents lists available at ScienceDirect

Carbon Resources Conversion

journal homepage: http://www.keaipublishing.com/en/journals/carbon-resources-conversion

# Carbon aerogels prepared by autocondensation of flavonoid tannin

A. Szczurek[a,b], V. Fierro[a], G. Medjahdi[c], A. Celzard[a,*]

[a] Université de Lorraine, CNRS, IJL, F-88000 Epinal, France
[b] LTNFM, Centre of New Technologies, University of Warsaw, Banacha 2c, 02097 Warsaw, Poland
[c] Université de Lorraine, CNRS, IJL, F-54000 Nancy, France

## HIGHLIGHTS

- The 1st carbon aerogels were prepared from gelation of tannins (T) catalysed by silica (S).
- Silica acted both as auto-condensation catalyst and as porogen.
- Dissolution of silica nanoparticles formed in the aerogels further increased their porosity.
- The influence of the S/T ratio and on the etching agent on the porosity was elucidated.
- Higher porosity and surface area than other tannin-based carbon aerogels are reported.

## ARTICLE INFO

*Keywords:*
Condensed tannins
Autocondensation reactions
Mesoporous carbons
Carbon aerogels

## ABSTRACT

The first carbon aerogels prepared by autocondensation of condensed (flavonoid) tannin, a cheap renewable resource extracted from Mimosa barks, are presented. Mixing aqueous solutions of tannin and sodium silicate indeed produced the very fast gelation of tannins, thus leading to organic hydrogels which were first converted into organic aerogels by supercritical drying, and then into carbon aerogels after pyrolysis at 900 °C. Subsequent dissolution of the silica nanoparticles thus formed within the carbon structure further increased significantly the porosity of the materials. Silica thus appeared to be both the gelation catalyst and a pore-directing agent. In this work, the influence on the porosity of the silica/tannin ratio and of the nature of the etching agent used for removing the silica was thoroughly investigated by combining several techniques. The conditions for producing either the most porous materials or those with the highest surface areas were identified and discussed.

## 1. Introduction

Carbons are materials of continuous interest, as proved by the huge number of papers published during the last decades. Actually, more and more of them are produced from formerly poorly valorised precursors, such as agricultural residues [1,2], low-quality coals [3,4], lignite [5], or wastes [6,7]. Out of low-cost precursors, condensed (flavonoid) tannins are considered as very effective for producing many thermoset polymeric materials and their carbonaceous derivatives. Tannin-based adhesives [8,9], foams [10,11,12], aero-, cryo- and xerogels [13,14,15,16,17], hydrothermal [18,19,20] and ordered mesoporous carbons [21,22,23,24] are well-known examples of versatile materials that can be prepared from tannins. Not only their structure can be tuned to fit a given application as adsorbent or as electrode material for example, but they constitute the best alternative to synthetic phenolic precursors such as resorcinol or phenol, the latter molecules being usual raw materials in the production of wood adhesives [25] and highly porous materials [26]. Their attractiveness is provided by the non-toxicity, low cost, and high reactivity of flavonoid tannins.

In some of the aforementioned applications, however, the materials synthesis requires using formaldehyde as a crosslinker. A lot of efforts have already been made to replace it by other reagents, including glutaraldehyde or glyoxal [27,28] and hexamethylenetetramine [29,30] for instance. They are definitely less harmful but present comparable or lower crosslinking efficiency than formaldehyde. In other works, neither aldehyde nor precursor of aldehyde was used, the oligomerisation and the crosslinking being due to the formation of –N = bridges between multi-aminated flavonoid units [18,31]. In a very recent paper, the tannin was condensed at very low pH, leading to crosslinker-free resins and then to porous carbons [32].

A safe and cheap way of tannin condensation was also proposed by Meikleham et al. [33]. In their work, the autocondensation of highly

* Corresponding author.
*E-mail address:* alain.celzard@univ-lorraine.fr (A. Celzard).

https://doi.org/10.1016/j.crcon.2019.02.001
Received 12 September 2018; Received in revised form 16 January 2019; Accepted 19 February 2019
Available online 20 February 2019
2588-9133/ © 2019 Production and hosting by Elsevier B.V. on behalf of KeAi Communications Co., Ltd. This is an open access article under the CC BY-NC-ND license (http://creativecommons.org/licenses/BY-NC-ND/4.0/).

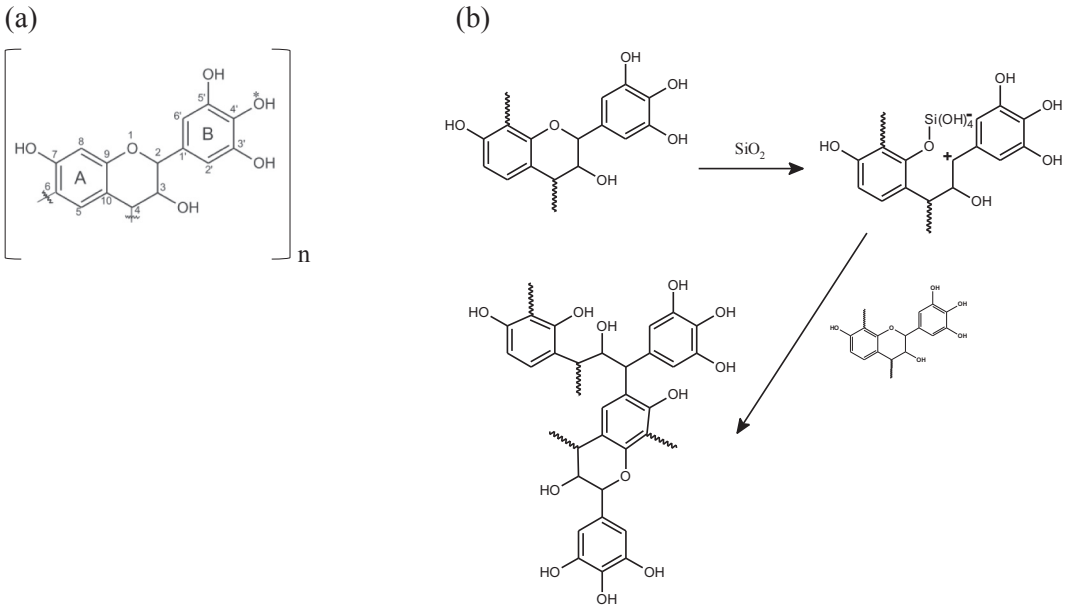


**Fig. 1.** (a) Chemical structure and atom numbering of prorobinetinidin, the main oligomer in mimosa tannin extract; (b) suggested (ionic) mechanism of the $SiO_2$-catalysed autocondensation of mimosa tannin (after [33]).

concentrated solution of tannin extract was catalysed by $SiO_2$ pre-dissolved in aqueous NaOH solution. The main reaction is shown in Fig. 1. The authors stated that autocondensation of tannin in the presence of $SiO_2$ takes place through a carbocation mechanism. In this reaction, $SiO_2$ links to the C2 of the flavonoid unit (see atom numbering in Fig. 1(a)), leading to the opening of the heterocycle. Intermolecular C2-C6/C2-C8 autocondensation thus occurs, as also proved for other (procyanidin and prodelphinidin) kinds of tannin [34]. In the case of mimosa tannin dominated by prorobinetinidin (see again Fig. 1(a)), the gelation is induced by acceleration of pyran rings opening reaction, visible by rapid and drastic increase of viscosity. Moreover, the carbocation participates also in C4-C8 or C4-C6 inter-flavonoid linkage, as it is known that hydride ion can be often extracted by it from the α – carbon to double bond or aromatic ring of another molecule. All these findings were examined, confirmed and discussed in detail in [33]. It has been shown later, however, that the first step of the aforementioned ionic mechanism involves the formation of radical species, whatever the kind of flavonoid tannin considered [35,36,37,38]. The practical application of resins based on autocondensed tannin in the production of wood particleboards was discussed elsewhere [39,40,41].

The present work was inspired by this technique for preparing highly mesoporous carbon materials with controlled textural properties. We show that total porosity and pore size distribution can be tuned by changing the amount of $Na_2SiO_3$ used both as catalyst of autocondensation and as mesopore-directing agent. The influence of etching the silica produced in the carbon materials on their final porous properties was also investigated.

## 2. Experimental

### 2.1. Synthesis

Organic gels were first prepared by simply mixing an homogeneous 11 wt. % aqueous solution of Mimosa tannin (kindly supplied by SilvaTeam, Italy) with different volumes of 35 wt. % aqueous solution of sodium silicate (also called “waterglass”) $Na_2SiO_3$ (Merck, Germany) in order to obtain $SiO_2$/tannin (S/T) mass ratios varying from 0.3 to 1.04. As the gelation of such prepared mixtures was quite fast, less than 2 minutes, the solution of $Na_2SiO_3$ had to be added quickly, i.e., in one single step. The samples were then cured for 3 h at room temperature and placed afterwards in polypropylene sealed bottles containing absolute ethanol. The latter was replaced 3 times by new one, in order to remove any residual water from the gels. Such exchange step was indeed required prior to supercritical drying in $CO_2$, using an Autosamdri-815 automatic critical point dryer (Tousimis, USA). After drying, the as-obtained aerogels were next heated at 5 °C $min^{-1}$ in a horizontal tubular furnace up to 900 °C, left for 2 h at the final temperature, and then slowly cooled down to room temperature. The whole process of heating and cooling took place in high-purity nitrogen flowing at 100 mL $min^{-1}$.

The resultant carbons aerogels were next divided in two parts: one part was washed with 2 mol $L^{-1}$ NaOH for 24 h in room conditions, while the second part was treated in the same conditions but with a 40 wt. % aqueous solution of HF. These washing steps were carried out for removing $SiO_2$ from the carbon matrices and thus for releasing some porosity. At the end, the samples were rinsed several times with distilled water until neural pH, and dried in a ventilated oven at 105 °C for 24 h. The harsh conditions of treatment caused cracking and the ruin of the initial monolithic shape of the gels. This is not a problem, however, since almost all applications of porous carbons are based on powders, and since the relevant features that these materials should present are surface area and pore volume, which are not related to the macroscopic structure.

It may be interesting to recall here that, despite HF aqueous solutions are dangerous and corrosive fluids, although widely used in the lab and in the industry, they are never released in the environment. Depleted solutions are indeed usually neutralised by precipitation in the form of $CaF_2$ (fluorite) by addition of calcium salts. Since $CaF_2$ is very poorly soluble, the amount of $F^-$ that is released is a few ppm only, far below the few hundred – few thousand ppm allowed in wastewater. Then, $CaF_2$ is recovered and can be treated for producing new fluorine compounds, as fluorite is indeed one of the raw materials of F chemistry.

### 2.2. Characterisation

The total porosity $\Phi$ (dimensionless) and the total pore volume $V_p$ ($cm^3$ $g^{-1}$) of the investigated porous materials were calculated by applying the following equations:

$$\phi = 1 - \frac{\rho_b}{\rho_s} \quad (1)$$

$$V_p = \frac{1}{\rho_b} - \frac{1}{\rho_s} \quad (2)$$

in which $\rho_b$ (g cm$^{-3}$) and $\rho_s$ (g cm$^{-3}$) are bulk and skeletal densities, respectively. As the materials were brittle and presented irregular shapes, $\rho_b$ was measured by mercury porosimetry, using an AutoPore IV 9500 device (Micrometrics, USA). For doing so, the volume of mercury introduced under vacuum into a sample holder of known, calibrated, volume, containing the sample, was measured at low pressure, 34.5 mbar. In such mild conditions, mercury neither intruded the pores of the material nor could collapse it, so its envelope volume could be deduced accurately. The skeletal density, $\rho_s$, was measured by helium pycnometry with an Accupyc II 1340 apparatus (Micromeritics, USA), using a known mass of finely crushed sample for avoiding any erroneous result due to possibly closed porosity. Helium being able to penetrate the narrowest pores, the volume of the carbon backbone was derived. Before all the aforementioned experiments, the samples were dried at 105 °C in vacuum overnight in order to avoid the distorting effect of adsorbed water on the volume measurements.

Nitrogen adsorption-desorption isotherms were obtained at −196 °C using an ASAP 2020 automatic adsorption apparatus (Micromeritics, USA). The samples were outgassed for 48 h under vacuum at 250 °C prior to any adsorption experiment. Surface areas, $A_{BET}$ (m$^2$ g$^{-1}$) were determined by the BET calculation method [42] applied to the adsorption branch of the isotherms within the adequate range of relative pressure ($P/P_0$). Particular attention was paid to the $C$ parameter in the BET equation that provides information about the interaction of the adsorbent surface and the adsorbate, and which has to be positive. $A_{BET}$ indeed strongly depends on the range of $P/P_0$ chosen to fit the BET equation to the nitrogen isotherm, and therefore it cannot be automatically applied between 0.05 and 0.25 relative pressures. We thus plotted $V_{N2} \times (1 - P/P_0)$, where $V_{N2}$ is the adsorbed nitrogen volume at a given value of $P/P_0$, as a function of $P/P_0$ and starting at $P/P_0 = 0.01$. The maximum $P/P_0$ to fit the BET equation is that where $V_{N2} \times (1 - P/P_0)$ reaches its maximum.

The micropore volume, $V_{DR}$ (cm$^3$ g$^{-1}$), was determined according to the Dubinin-Raduskevich method [43]. The total pore volume, sometimes referred to as the Gurvitch volume, $V_{0.97}$ (cm$^3$ g$^{-1}$), was defined as the volume of liquid nitrogen corresponding to the amount adsorbed at a relative pressure $P/P_0 = 0.97$ [44]. The average micropore diameter, $L_0$ (nm), was calculated from either Stoeckli's equation (Eq. (3)) [45] or Dubinin's equation (Eq. (4)) [46] when $E_0$ (kJ mol$^{-1}$) was lower than 20 kJ mol$^{-1}$. $E_0$ is the characteristic adsorption energy of probe molecules, derived from the nitrogen adsorption isotherms at −196 °C by application of the Dubinin–Raduskevich method.

$$L_0 = \frac{10.8}{E_0 - 11.4} \quad (3)$$

$$L_0 = \frac{24}{E_0} \quad (4)$$

The pore size distributions (PSDs) in the whole range of pore sizes were obtained using non-local density functional theory (NLDFT) from the Solution of Adsorption Integral Equation Using Splines (SAIEUS®) routine. This method has the advantage of combining both $CO_2$ and $N_2$ adsorption data to get more accurate PSDs [47]. Moreover, it allows fitting the PSDs with a spline model, avoiding the usual singularities of the classical DFT model. The smoothing parameter λ was set constant and equal to 2.75 for all samples in order to allow comparing different PSDs. The micropore volume (pores diameters < 2 nm), $V_{\mu\ NLDFT}$ (cm$^3$ g$^{-1}$), was calculated by integrating the PSD up to 2 nm, the ultramicropore volume (pores diameters < 0.7 nm), $V_{u\mu\ NLDFT}$ (cm$^3$ g$^{-1}$), was calculated by integrating the PSD up to 0.7 nm, and the supermicropore volume (pores diameters between 0.7 and 2 nm) was obtained as $V_{s\mu\ NLDFT} = V_{\mu\ NLDFT} - V_{u\mu\ NLDFT}$. The mesopore volume, $V_{meso}$ (cm$^3$ g$^{-1}$), was assumed to be the difference $V_{0.97} - V_{DR}$. The NLDFT method was also used to determine surface area, $S_{NLDFT}$ (m$^2$ g$^{-1}$), by integrating the PSDs over the whole range of pore sizes [48].

Finally, the PSDs in the mesopore range were calculated by application of the BJH model [49] with the the Kruk–Jaroniec–Sayari (KJS) correction [50] supplied by Micromeritics software, considering the desorption branches. The BJH pore size model is based on the classical Kelvin equation modified for multi-layer adsorption on the pore wall prior to the onset of condensation or after completing evaporation, and is widely used to investigate the pore-size distribution of meso- and partly macroporous materials.

Due to some limitations of the BJH model, underestimation of pore sizes may happen, hence the mesoporosity was also probed by mercury intrusion. The latter was carried out with the same apparatus as for measuring the bulk density. The experiments were performed in two steps: first in a low-pressure chamber within the pressure range 0.001–0.24 MPa; then the sample holder filled with sample and mercury was transferred to a high-pressure chamber in which the pressure was increased from 0.24 to 414 MPa. The pore size distributions were estimated by application of Washburn's equation, assuming cylindrical pores:

$$D = -\frac{4\gamma cos\theta}{P} \quad (5)$$

where $D$ (nm) is the pore diameter, γ (0.485 N m$^{-1}$) is the surface tension of mercury, $\theta$ (usually fixed at 140°) is the contact angle between mercury and the material, and $P$ (Pa) is the intrusion pressure. Eq. (5) shows that the narrowest pores available to Hg have a diameter of 3.6 nm.

The morphology of three groups of samples: (i) not treated; (ii) treated with NaOH; and (iii) treated with HF, was investigated by scanning electron microscope (SEM) observations, using a FEI Quanta 600 FEG. For all samples, both detectors of secondary electrons (SE) and backscattered electrons (BSE) were used to obtain the most detailed images. SE indeed provide best evidence of the topological contrast while BSE were used for visualising the chemical contrast and were then helpful at the moment of performing energy-dispersive X-ray analysis (EDX) of the samples.

The intimate materials structure was observed with a FEI CM200 transmission electron microscope (TEM), using electrons of energy 200 keV in bright field mode. Prior to the observations, powdered samples were ultrasonically dispersed in ethanol and transferred onto a 200 mesh carbon-coated copper grid. The pore diameters were measured from calibrated micrographs using ImageJ software. Around 50 measurements were thus made for each observed sample, and the obtained values of pore diameters were averaged.

X-ray diffraction (XRD) profiles of carbon materials treated with HF were obtained with a PANalytical X'Pert Pro diffractometer (Philips, The Netherlands). The latter was used in a Bragg–Brentano configuration in reflection, and was equipped with a Cu ($K_\alpha$ radiation) anticathode and a high-speed multichannel X'Celerator detector. The carbon gels were ground in an agate mortar, and the resultant powders were placed on the sample holder. The latter was installed on a rotating spinner for allowing the highest number of grains to be in diffraction position. The interplanar spacing $d_{002}$ (nm) was calculated from the well-known Bragg's law, whereas the sizes of the coherent domains along $a$ and $c$ axes, $L_a$ (nm) and $L_c$ (nm), respectively, were calculated from the 10$l$ and 0 0 2 reflections, respectively, using modified Scherrer's equation [51,52]:

$$L = \frac{K\lambda}{Bcos\theta} \quad (6)$$

where $K$ is a factor, 1.85 for $L_a$, and 0.9 for $L_c$, λ is the wavelength, here 0.154036 nm, $B$ is the FWHM of the 10$l$ reflection for $L_a$ and of the 0 0 2 reflection for $L_c$. Finally, the average number of aromatic layers, $N_c$, was

obtained from the interlayer spacing, $d_{002}$, and the coherent domains along the c axis, $L_c$, according to:

$$N_c = \frac{L_c}{d_{002}} \quad (7)$$

## 3. Results and discussion

### 3.1. Tannin-derived carbons

The conversion of tannin into carbon has been already addressed in detail in former works from our group (see for instance [10,15,16,18,53,54,55,56,57,58]. Our Raman spectroscopy and XPS analyses [17,23,24,32,59,60] have clearly shown that tannin-based carbon is mainly aromatic (i.e., sp2) but non-graphitic, based on nanometre-size domains bordered by sp3 carbon atoms, and that around 60% of the carbon is type I (hydrocarbons, aromatics, aliphatics), around 25% is type II (Csp3 and C—O bonds associated to ethers, phenols and anhydrides), the rest being types III (C═O bond in carbonyls and quinones) and IV (C-O bonds in carboxyl acids) at levels of a few % of each.

The elemental composition of the tannin used here has been published before [61] and is as follows: C (53.8 wt%), H (5.4 wt%), N (0.6 wt%), S (0.1 wt%) and O (40.1 wt%). This tannin and its resins, whether crosslinked or condensed, are also well-known to have a carbon yield of *ca.* 45% [62], a value also recovered here after silica was leached out. After pyrolysis, the carbon content, which has been measured multiple times (see references above about tannin-derived carbons) always range from 85 to above 95 wt.% after pyrolysis at 900 °C, depending on the level of mineral impurities, just as observed in the present work (see below).

### 3.2. Porous texture

The results of bulk density, total porosity, and corresponding total pore volume of samples treated with NaOH and HF are presented in Table 1. It can be seen that these quantities can be controlled by the $SiO_2$/tannin (S/T) mass ratio, irrespective to the nature of the etchant that was used. More $Na_2SiO_3$ in the reaction mixture resulted in more porous final carbons, as expected. Another logical finding is that treating the carbon aerogels in the most aggressive environment, HF, led to the most efficient removal of the silica, thus producing samples of much higher porosity and associated porous volumes. It is indeed a well-established fact that HF is much more efficient than NaOH for dissolving silica, and this is even truer as soon as big silica particles are considered, whose existence in the form of clusters was confirmed (see below and next section).

As suggested by Fig. 2, showing the relative changes of porous parameters when using HF as etchant with respect to NaOH, no significant difference was observed for samples prepared with S/T mass ratios within the range 0.3–0.75. In contrast, the sample prepared with the highest mass ratio, 1.04, had a relatively much lower density caused

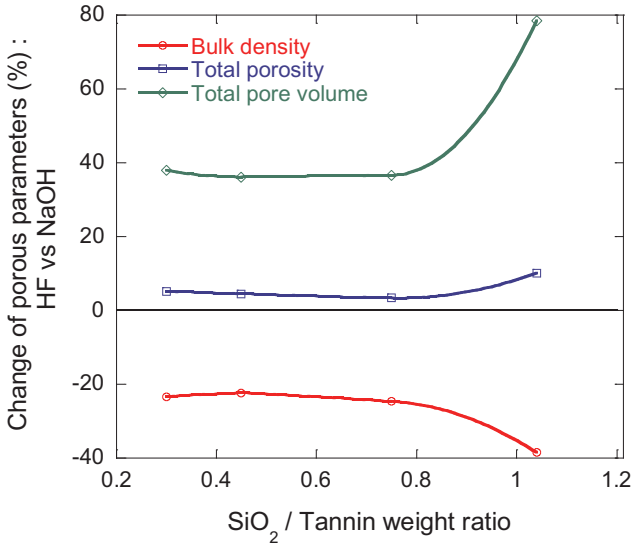


**Fig. 2.** Changes of porous parameters when using HF as etchant with respect to NaOH. The curves are just guides for the eye.

by the removal of $SiO_2$ clusters not accessible to, or not soluble in, NaOH. As a result, HF produced more porous samples at high S/T ratio, since the total pore volume was almost 80% higher than when NaOH was used. NaOH can indeed be enough for dissolving truly small (nano) particles, but as far as clusters are concerned, HF always performs better. As a result, the porosity of silica-rich materials can be much more developed by using HF.

The nitrogen adsorption-desorption isotherms of carbon aerogels treated with either NaOH or HF are given in Fig. 3. All such isotherms were combinations of type I and type IVa according to the IUPAC classification, thus evidencing the presence of both micro- and mesoporosity. The type IVa was accompanied by hysteresis loops, corresponding to capillary condensation and presenting intermediate shapes between types H2(b) and H5 [63]. The stepwise desorption branches suggest that these carbons present bimodal porosity associated with certain pore structures containing both open and partially blocked mesopores. This type of desorption isotherms can be observed when pore network effects occur, i.e., when large pores have to be emptied through narrower pores connecting them to the outer surface of the material. In this case, those large pores are emptied at lower pressure than open pores of comparable diameter.

Fig. 3 also suggests shows that more sodium silicate in the initial formulation produced less microporous carbon aerogels after removal of the silica, whereas the mesoporosity passed through a maximum. Indeed, by considering the adsorbed $N_2$ volume at low relative pressure, it can be seen that the height of the plateau decreased, on average, when the S/T ratio increased. This phenomenon is accompanied by a widening of the micropore size distribution, as revealed by the slight

**Table 1**
Porous properties of $SiO_2$-Tannin (SIOT) samples treated with either NaOH or HF.

| Sample | S/T mass ratio | Bulk density[a] (g cm$^{-3}$) | | Total porosity[b] (%) | | Total pore volume[c] (cm$^3$ g$^{-1}$) | | Intrusion volume[a] (cm$^3$ g$^{-1}$) | |
|---|---|---|---|---|---|---|---|---|---|
| | | NaOH | HF | NaOH | HF | NaOH | HF | NaOH | HF |
| SIOT30 | 0.30 | 0.77 | 0.59 | 67.3 | 70.8 | 0.87 | 1.20 | 0.54 | 0.78 |
| SIOT45 | 0.45 | 0.67 | 0.52 | 70.6 | 73.8 | 1.05 | 1.43 | 0.69 | 1.05 |
| SIOT75 | 0.75 | 0.65 | 0.49 | 73.4 | 75.9 | 1.12 | 1.53 | 0.79 | 1.37 |
| SIOT104 | 1.04 | 0.52 | 0.32 | 74.8 | 82.4 | 1.44 | 2.57 | 1.30 | 2.37 |

[a] Obtained from Hg porosimetry.
[b] Obtained from Eq. (1).
[c] Obtained from Eq. (2).

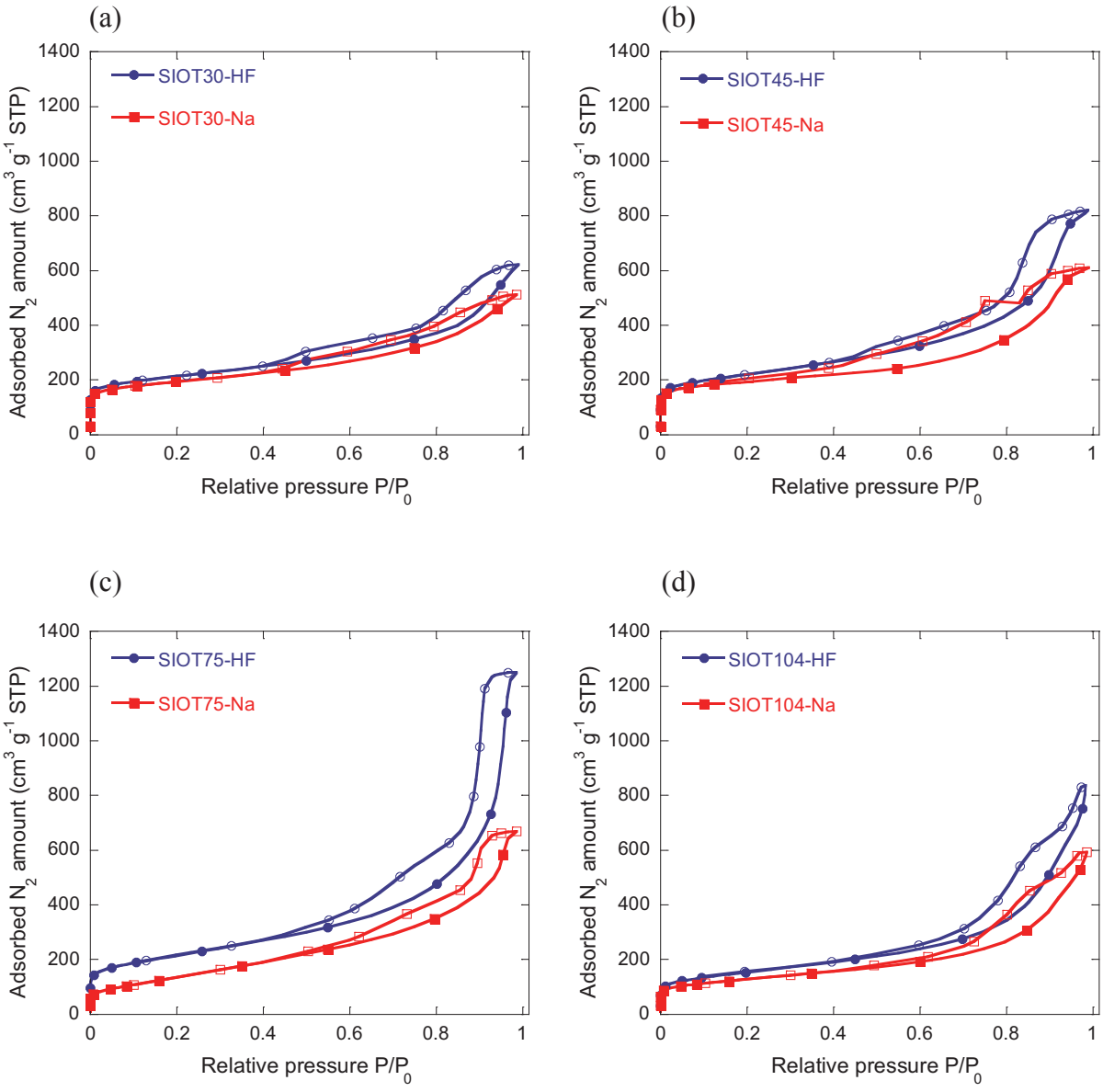


**Fig. 3.** $N_2$ adsorption-desorption isotherms (filled and empty symbols, respectively) of $SiO_2$-Tannin (SIOT) samples treated with either NaOH or HF and containing various initial S/T mass ratios: (a) 0.30; (b) 0.45; (c) 0.75; and (d) 1.04.

**Table 2**
Results of $N_2$ adsorption measurements.

| Sample | $A_{BET}$ ($m^2\ g^{-1}$) | | $S_{NLDFT}$ ($m^2\ g^{-1}$) | | $V_{0.97}$ ($cm^3\ g^{-1}$) | | $V_{DR}$ ($cm^3\ g^{-1}$) | | $L_0$ (nm) | | $V_{meso}$ ($cm^3\ g^{-1}$) | | $V_{\mu\ NLDFT}$ ($cm^3\ g^{-1}$) | | $V_{u\mu\ NLDFT}$ ($cm^3\ g^{-1}$) | | $V_{s\mu\ NLDFT}$ ($cm^3\ g^{-1}$) | |
|---|---|---|---|---|---|---|---|---|---|---|---|---|---|---|---|---|---|---|
| | Na | HF | Na | HF | Na | HF | Na | HF | Na | HF | Na | HF | Na | HF | Na | HF | Na | HF |
| SIOT30 | 701 | 770 | 791 | 836 | 0.76 | 0.91 | 0.27 | 0.29 | 0.92 | 0.99 | 0.54 | 0.68 | 0.22 | 0.23 | 0.16 | 0.16 | 0.06 | 0.07 |
| SIOT45 | 709 | 783 | 777 | 832 | 0.92 | 1.23 | 0.28 | 0.30 | 1.04 | 1.13 | 0.71 | 1.02 | 0.21 | 0.21 | 0.14 | 0.13 | 0.07 | 0.08 |
| SIOT75 | 497 | 759 | 445 | 739 | 1.00 | 1.87 | 0.14 | 0.29 | 1.20 | 1.25 | 0.93 | 1.71 | 0.07 | 0.16 | 0.04 | 0.08 | 0.03 | 0.08 |
| SIOT104 | 451 | 542 | 460 | 504 | 0.81 | 1.11 | 0.17 | 0.21 | 1.21 | 1.34 | 0.70 | 0.99 | 0.11 | 0.12 | 0.06 | 0.04 | 0.05 | 0.08 |

broadening of the knee of the $N_2$ adsorption branch at low $P/P_0$. As for the mesoporosity, the width of the hysteresis loop unambiguously increased from S/T = 0.3 to 0.75, and decreased at S/T = 1.04. However, the final total porosity of those aerogels, corresponding to the adsorbed amount at saturation, did not change proportionately with the amount of silica initially introduced. Especially in the case of samples etched with NaOH, the adsorbed volume of $N_2$ at saturation remained in the range 500–600 STP $cm^3\ g^{-1}$, irrespective to the S/T ratio. This finding suggests that a significant part of the porosity was already pre-existing in the carbon aerogels.

Besides, Fig. 3 shows that, at constant initial amount of $Na_2SiO_3$, etching with HF led to more porous carbon aerogels than with NaOH. Indeed, HF can dissolve silica particles of any size, unlike NaOH, thus, as soon as clusters are dissolved by HF, formerly inaccessible silica nanoparticles become available and in turn can be dissolved consequently. This effect is observed not only by the higher adsorbed volume

of $N_2$ at saturation, but also by the higher plateau at low relative pressure. As a result, both micro and mesoporosity were developed upon silica dissolution. All the data of porous texture, corresponding to results of $N_2$ adsorption measurements for SIOT-Na and SIOT-HF samples are gathered in Table 2 and are discussed below.

HF systematically led to higher values of porous texture parameters, whether these are surface area, micro and mesopore volumes, or average micropore width. For instance, the surface areas were in the ranges 450–710 $m^2\ g^{-1}$ and 540–780 $m^2\ g^{-1}$ for samples treated with NaOH and HF, respectively. Thus, HF induced an increase of $A_{BET}$ of around 10–20% in comparison to analogue samples treated with NaOH. Again, this finding is easily explained by the higher ability of HF to dissolve big silica particles blocking the access to nanoparticles buried in the bulk of the carbon material. As soon as clusters are leached out, nanoparticles become available and can be etched. Consequently the surface area, mainly due to very narrow pores, can increase significantly. The $S_{NLDFT}$ was quite similar to $A_{BET}$, with differences lower than 10%. $A_{BET}$ underestimates the surface area when pores narrower than 0.7 nm exist. In the same way, $V_{DR}$ overestimates the microporosity, and was only given herein for comparison purposes with other studies reported in the literature.

All micropore volumes (whether total or subdivided into ultra- and supermicropores) decreased, on average, with the amount of silica, and so did the surface areas. Such a decrease led to a rise of mesopore fraction, up to 93% and 91% for SIOTs-Na and SIOTs-HF, respectively. However, the mesopore volumes, $V_{meso}$, and hence the total pore volumes measured by adsorption, $V_{0.97}$, passed through a maximum at S/T = 0.75. Such maximum is likely due to the formation of silica clusters which are difficult to eliminate at too high S/T mass ratios. Those clusters produced broader pores, leading to the observed decrease of surface area and pore volumes, even when using HF, which proved to be more efficient that NaOH in all cases. The presence of such clusters was confirmed by SEM observation (see next section), and was also suggested by the way the average micropore width, $L_0$, changed with the S/T ratio of samples etched with either HF or NaOH, see Fig. 4. Indeed, whereas the $L_0$ of SIOTs-HF samples continuously increased with the S/T ratio, a clear saturation is seen for SIOTs-Na samples above S/T = 0.75 due to blocking of pores by $SiO_2$ nanoparticles.

It is also worth noticing that carbon gels prepared in the way described here present significantly higher pore volumes than those of tannin-based carbon gels having comparable BET area but prepared from classic polycondensation with formaldehyde. For instance, the results given in Table 2 show that formaldehyde-free carbon aerogels prepared with silica acting both as autocondensation catalyst and porogen, and treated with HF afterwards, are much more mesoporous than their counterparts made with formaldehyde and without silica [55]. Besides, their BET area is also higher, on average, despite their microporosity is lower. This is an excellent characteristic, given that aerogels are generally much sought after for their exceptionally large and almost purely mesopore volume. The same applies to formaldehyde-derived cryogels, whose micro and mesopore volumes, BET areas and average micropore widths, are lower than the present materials etched with HF [56].

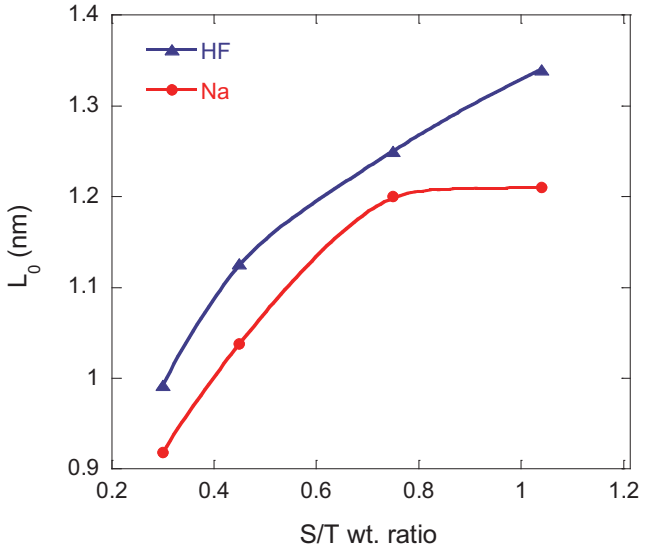


**Fig. 4.** Changes of average micropore width of samples etched with either HF or NaOH, as a function of the initial S/T mass ratio in the formulation.

For SIOTs-Na and SIOTs-HF samples, the microporosity ($V_{\mu\ NLDFT}$) represents 7–29% and 9–25% of the porosity measurable by adsorption ($V_{0.97}$), respectively. The part of the microporosity corresponding to ultramicropores ($V_{u\mu\ NLDFT}$) was the highest at low S/T ratio and decreased when the latter increased, as seen by the micro/mesopore-size distributions shown in Fig. 5 according to two ways: the usual way on the one hand, i.e., $\partial V/\partial w$ versus $w$, where $V$ is the pore volume and $w$ is the pore width, and the "log differential" way on the other hand, i.e., $\partial V/\partial \log w$ versus $w$. The latter presentation is known to emphasise the pores of higher diameters, which otherwise would be hardly visible [64].

When S/T increased, the intensity of the narrow and high peak centred on 0.45–0.58 nm, depending on the material (see Fig. 5(a) and (c)), indeed decreased significantly, whatever the etching agent. The increased amount of autocondensation catalyst indeed improved the crosslinking of the polymeric matrix and reduced the evolution of gases during pyrolysis that produces microporosity. For this reason, $V_{u\mu\ NLDFT}$, $V_{s\mu\ NLDFT}$ and $V_{\mu\ NLDFT}$ all decreased when increasing the S/T ratio. At the same time, a population of mesopores centred on ~4–24 nm increased with S/T, with a maximum at 0.75 as observed above. For some samples, additional small peaks centred on ~1 nm could be also observed, but with no certainty as to their significance, due to some known biases of the DFT method near 1 nm. The present gels can thus be considered as roughly bimodal in the range of micro- to mesoporosity.

The BJH model was applied to the desorption branches of $N_2$ sorption isotherms for obtaining more detailed information about mesopores, and the corresponding results are presented in Fig. 6. SIOT-Na samples presented one main asymmetric peak centred on ~5 nm for S/T ratios of 0.3, 0.45 and 0.75, and one centred on ~10 nm for S/T = 1.04. The height of those peaks decreased when the S/T ratio increased, but as the distribution broadened at the same time, it led to an increase of mesopore volume until S/T = 0.75, as observed in Table 2. For the latter ratio, the distribution was clearly bimodal, with a second peak centred on ~21 nm. The samples SIOT-HF were different in the sense that, except SIOT104-HF, all presented bimodal distributions, and the position of their two major peaks moved with the S/T ratio. Thus, the samples prepared with S/T = 0.3 and 0.45 had almost similar identical distributions, except the corresponding absolute pore volumes, whereas samples with higher S/T had peaks visibly shifted towards higher pore sizes. At the highest S/T mass ratio, the distribution was much broader until only one broad peak remained. Such distribution was nearly exactly the same for both SIOT104-HF and SIOT104-Na, suggesting that the nature of the etching effect had no more influence on the mesoporosity above a critical amount of silica in the initial formulation.

The mesoporous and macroporous structure of SIOTs samples investigated by mercury porosimetry led to the intrusion curves vs. pore diameters presented in Fig. 7, whereas the values of total intrusion volumes were already provided in Table 1. The intrusion volumes increased with the S/T mass ratio for both types of materials, but those of the SIOTs-HF samples increased the most. This finding again suggests that NaOH was as not as efficient as HF for producing porosity at high S/T values.

Whether etched with NaOH or HF, it can be seen that a low fraction

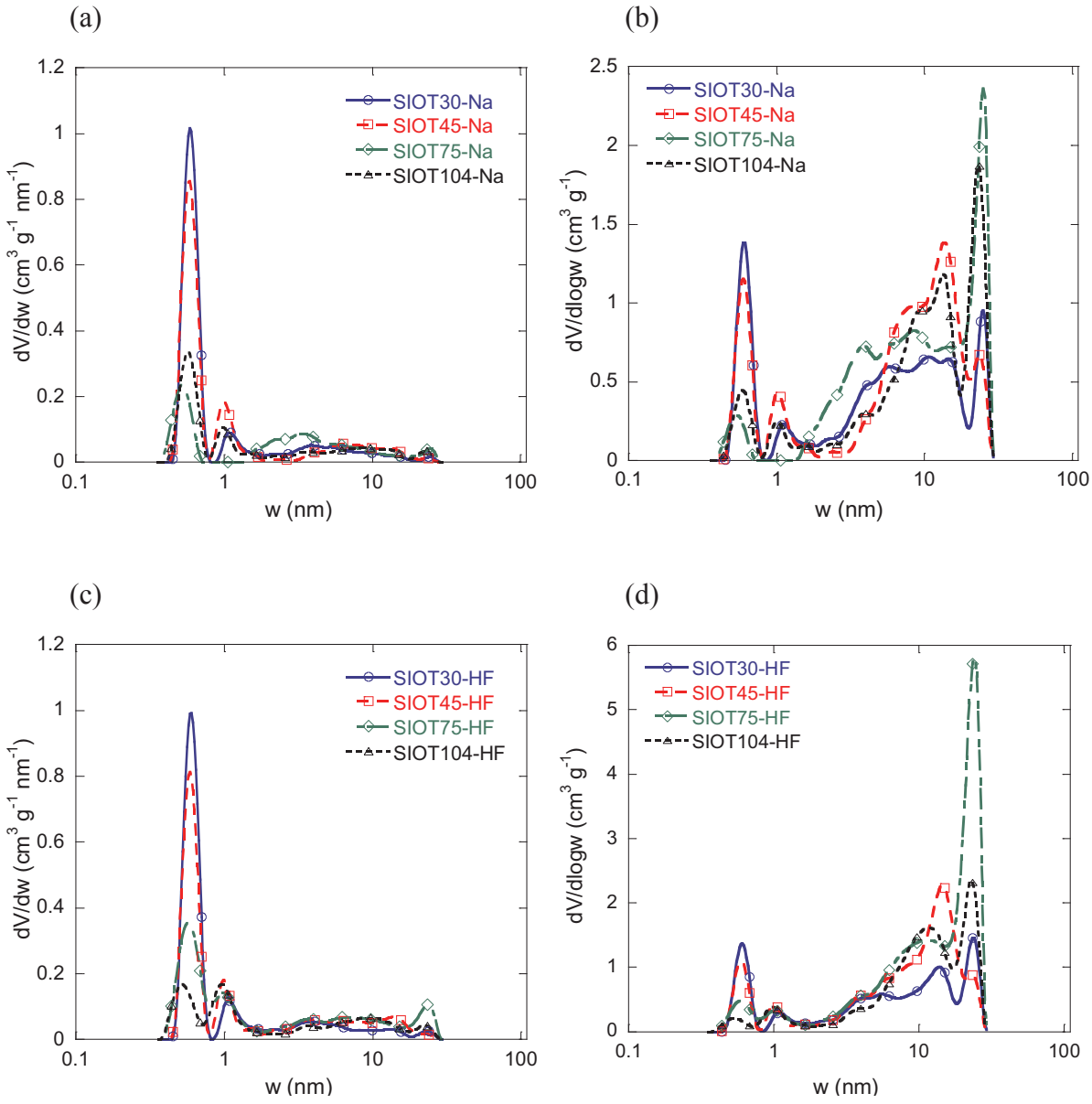


**Fig. 5.** Micro/mesopore size distributions of samples of various S/T ratios and treated with either: (a-b) NaOH, or (c-d) HF, calculated by application of the NLDFT method: (a) and (c) are differential distributions, whereas (c) and (d) are log differential distributions.

of macropores and of large mesopores is produced, and that most of the porosity that was released corresponds to mesopores smaller than 22 nm. Indeed, at such value of diameter, the intruded volume increases sharply. This finding suggest that only a few big silica particles (roughly in the range ~5–320 μm) were present in the carbon gels, whereas most of the silica existed as particles with sizes ~4–22 nm. Among the latter, two populations could even be deduced: ~4–6 nm and ~6–22 nm. The mesoporous structure of SIOT materials thus presented a bimodal character in this range of porosity, which was confirmed by adsorption results based on the BJH model. The corresponding pore-size distributions deduced from Fig. 7 are presented in Fig. 8, and obvious similarities with the former Fig. 6 can be seen.

Fig. 8 shows that the PSDs of both kinds of samples, SIOTs-Na and SIOTs-HF, are nearly the same, exhibiting the bimodal character expected from Fig. 7 with two main peaks centred in the ranges ~6–9 nm on the one hand, and ~12–50 nm on the other hand. For the lowest S/T mass ratio, 0.30, HF removed a higher fraction of bigger silica nanoparticles, leading to a peak of higher intensity in the PSD, and removed smaller silica nanoparticles, thus shifting the corresponding peak maximum to lower values of pore diameter. This phenomenon is explained by the opening of the narrowest mesopores formerly blocked by bigger $SiO_2$ particles. As a support of such assumption, the peak at high pore diameters became broader and asymmetric, and its maximum was shifted to even higher diameters. Concerning the samples SIOT75 and SIOT104, the peaks occurred exactly at the same positions whether HF or NaOH was used, but HF etching again increased the corresponding pore volumes. This indicates that S/T mass ratios higher than 0.75 resulted in the agglomeration of $SiO_2$ particles and created the macroporous structure of the carbon gels.

### 3.3. Morphology

The morphology of carbons before and after etching with NaOH or HF is shown in Fig. 9. The surface of raw carbon aerogels was found to be covered by 1–10 μm round-shaped deposits of $SiO_2$ particles, see Fig. 9(a), which could definitely not account for the nanoporous structure of the materials. The etching in NaOH or HF was intended to remove the silica and consequently to open the porous structure, but in

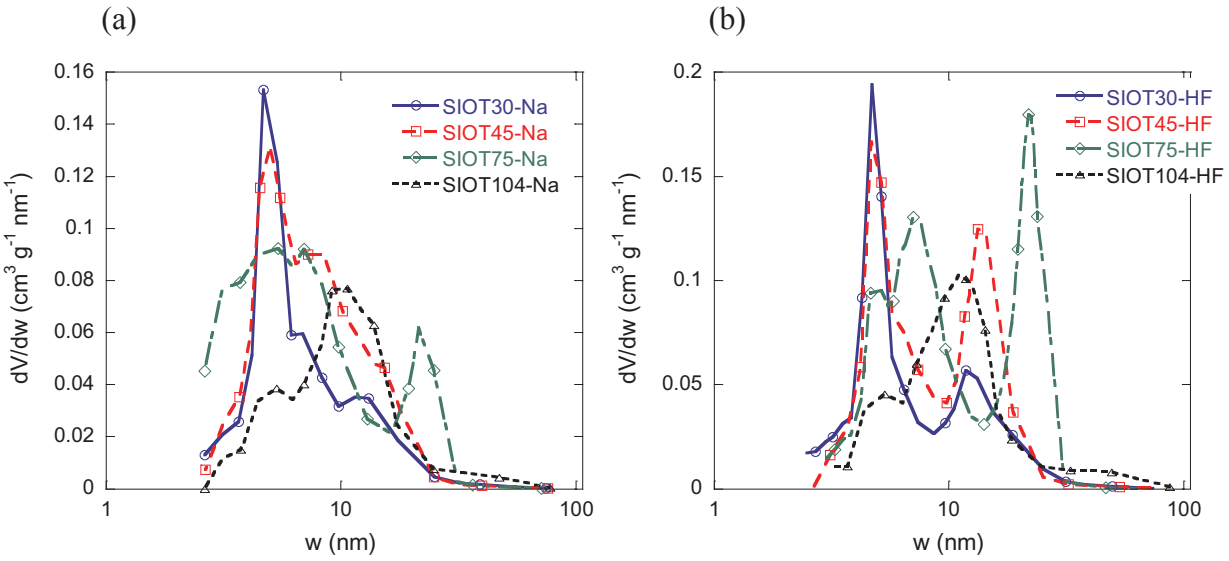


**Fig. 6.** Pore size distributions obtained by application of the BJH model to the desorption branches of $N_2$ isotherms for samples etched with: (a) NaOH, and (b) HF.

the case of NaOH, the process was not sufficient for samples with high S/T mass ratio: a large amount of the $SiO_2$ was indeed left in the carbon structure, as clearly seen by the white inclusions in Fig. 9(b). In contrast, the HF etching resulted in neat carbon materials without visible traces of $SiO_2$, see Fig. 9(c).

As for the latter, two distinct surface aspects were observed, with an outer uniform and rather smooth skin, or with the fine nodular structure usually found in carbon gels. The typical size of those nodules was in the range 30–100 nm, i.e., typical of other carbon aerogels based on tannin [55].

EDX analysis was carried out in order to estimate the concentrations of elements present on the surface of carbon aerogels before and after each kind of etching. The results are presented in Fig. 10 for SIOT104 before and after etching with HF. The pyrolysis of organic aerogels loaded with sodium silicate resulted in carbon materials fully covered and/or impregnated with silica compounds. Elemental mapping shows that Si (green in Fig. 10(a)) was closely associated with O (turquoise blue), and that Na (dark blue) was very well dispersed. Some red islands could also be observed, associating C and Si, likely to correspond to the SiC phase. The presence of SiC was confirmed by quantifying the local concentrations of elements in those red areas: C and Si elements were indeed much more abundant than elsewhere. Finding SiC is not surprising as it was previously shown that, for instance, carbonisation of rice straw containing up to 20 wt. % of $SiO_2$ also leads to carbon materials containing small inclusions of silicon carbide [65,66]. The etching led to carbon materials with traces of Si and Na in amounts 0.14 and 0.02 wt. %, respectively, see Fig. 10(b). However, EDX is only a semi-quantitative method, so those amounts are subject to non-negligible uncertainty.

EDX carried out on SIOT104 sample etched with NaOH (not shown) led to rather similar results (C: 91.54 at.%; Na: 0.02 at.%; O: 5.47 at.%) although with a higher amount of silica (2.96 at.%, compare with Fig. 10(b)), proving once more that NaOH is not as efficient as HF when used as etching agent. Such low amount of silica is due to the fact that $SiO_2$ dissolution proceeds from the surface to the inner part of the material. EDX being a surface analysis, it cannot account for the bulk silica content, which was expected to be significantly higher than in the sample etched with HF.

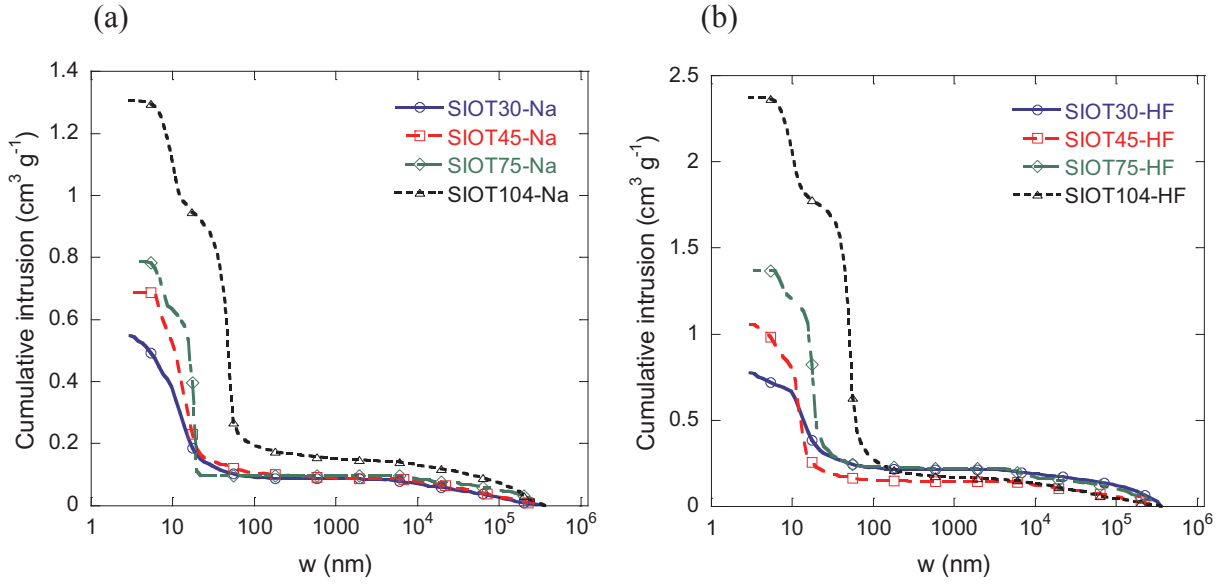


**Fig. 7.** Hg intrusion curves for samples of various S/T ratios and treated with either: (a) NaOH, or (b) HF.

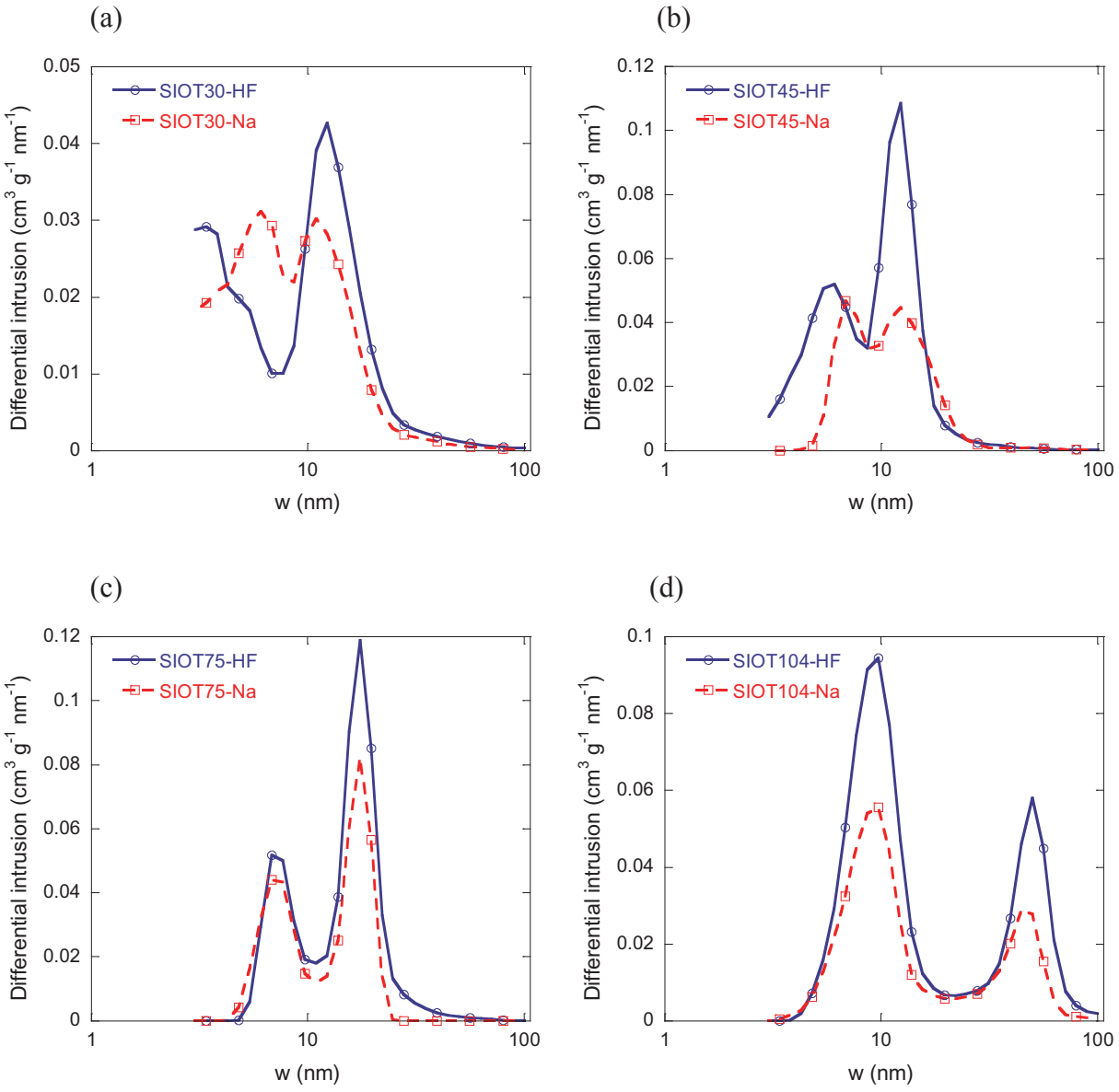


**Fig. 8.** Pore-size distributions deduced from the data of Hg porosimetry shown in Fig. 7.

TEM observations were also performed in order to investigate both the porous structure and the morphology of the carbon aerogels. The corresponding pictures are given in Fig. 11. At the lowest magnification, a well-developed porous structure is clearly visible in the form of spherical or round-shaped pores. Such pores result from the dissolution of silica nanoparticles. The measurements carried out with ImageJ software revealed that their average diameters are within the range ~5–50 nm, in agreement with the aforementioned results of adsorption treated with the BJH model, and also with the pore size distributions derived from Hg porosimetry. At higher magnification, TEM evidenced the highly disordered texture of the carbon material, as expected when using a phenolic molecule such as tannin as carbon precursor.

XRD patterns are shown in Fig. 12. All samples (treated with HF) produced nearly the same XRD profiles, with the 0 0 2 reflection appearing as a broad shoulder with a maximum at Bragg angle 2θ–20–23° (see the precise values in Table 3). The presence of such broad reflection reveals the existence of crystallites of quite limited size ($L_c$) perpendicular to the aromatic layers. The values of $L_c$ calculated from Eq. (6) decreased from 1.19 to 0.91 nm when the S/T mass ratio increased (see Table 3). The order of magnitude of such values is in complete agreement with what has been reported earlier for other tannin-based carbons, as explained in Section 3.1. The 10$l$ (2θ = 44°) and 11$l$ (2θ = 80°) peaks appeared as reflections both broad and of low intensity. The corresponding values of $L_a$ calculated again from Eq. (6) but accounting for the crystallite size along the aromatic layers decreased from 2.59 to 1.97 nm when the S/T mass ratio increased (Table 3).

The interlayer spacing $d_{002}$ had values ranging from 0.383 to 0.436 nm, and thus was much higher than that of perfect hexagonal graphite (0.335 nm). Finally, the average number of aromatic layers, $N_c$, was calculated according to Eq. (7). The values of $L_a$, $L_c$, $d_{002}$ and $N_c$ are also given in Table 3. All these data further confirm that the present carbon aerogels were highly disordered, and that the disorder of the carbon texture increased further with the initial amount of sodium silicate in the formulation.

## 4. Conclusion

The present work focused on synthesis and investigation of carbon aerogels prepared by autocondensation reaction of flavonoid tannin

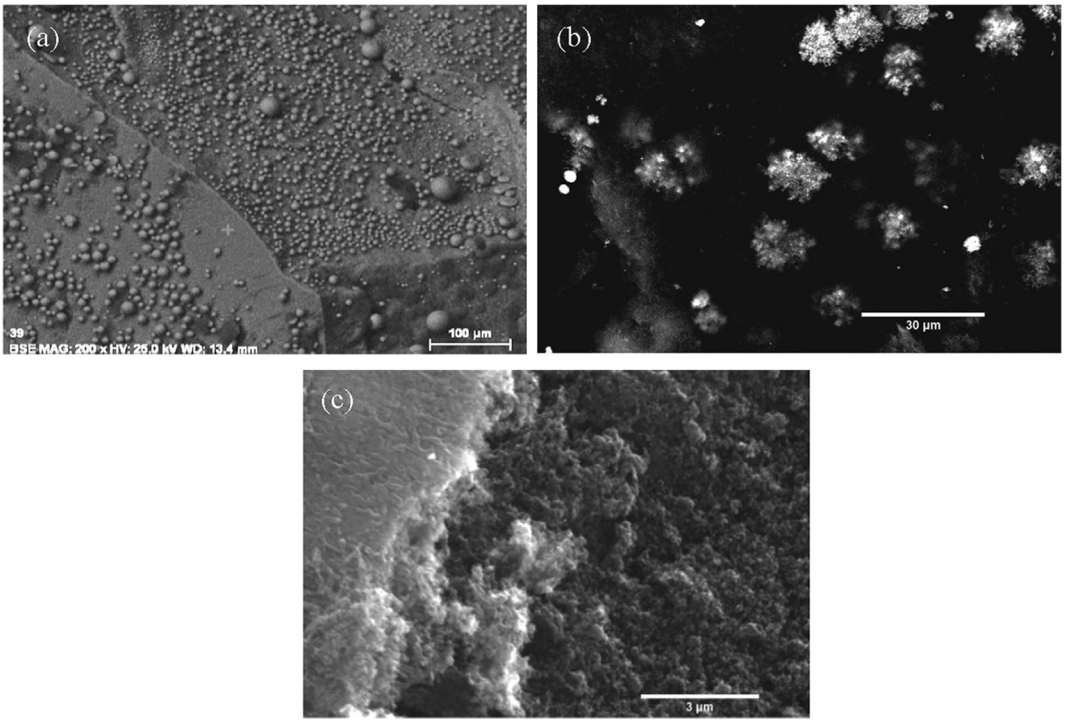


**Fig. 9.** Morphology of SIOT carbon aerogels having the highest initial S/T ratio, SIOT104: (a) before; and after etching with: (b) NaOH and (c) HF. Images (a) and (b) were obtained with the backscattered electron detector, whereas (c) was obtained with the secondary electron detector.

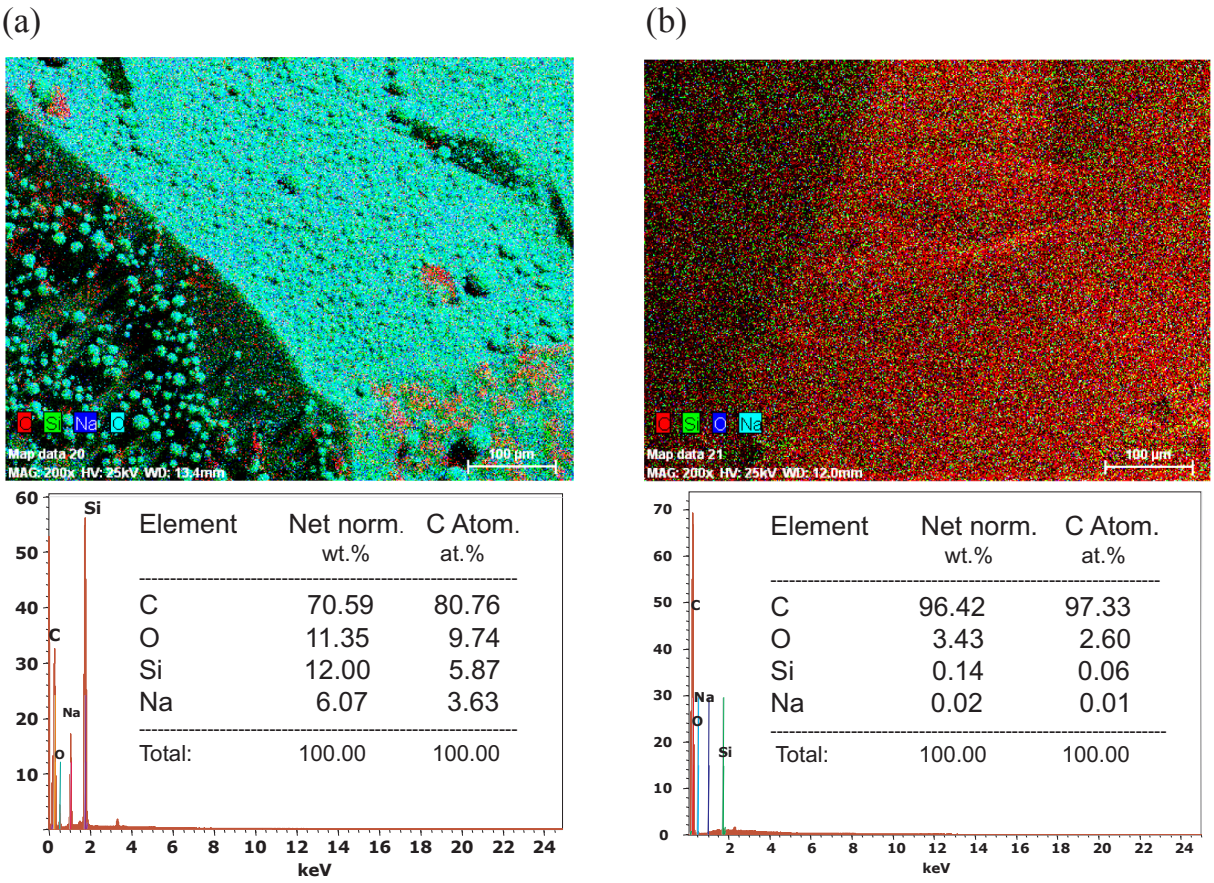


**Fig. 10.** EDX analysis of the sample having the highest initial S/T ratio, SIOT104: (a) before; and (b) after etching with HF.

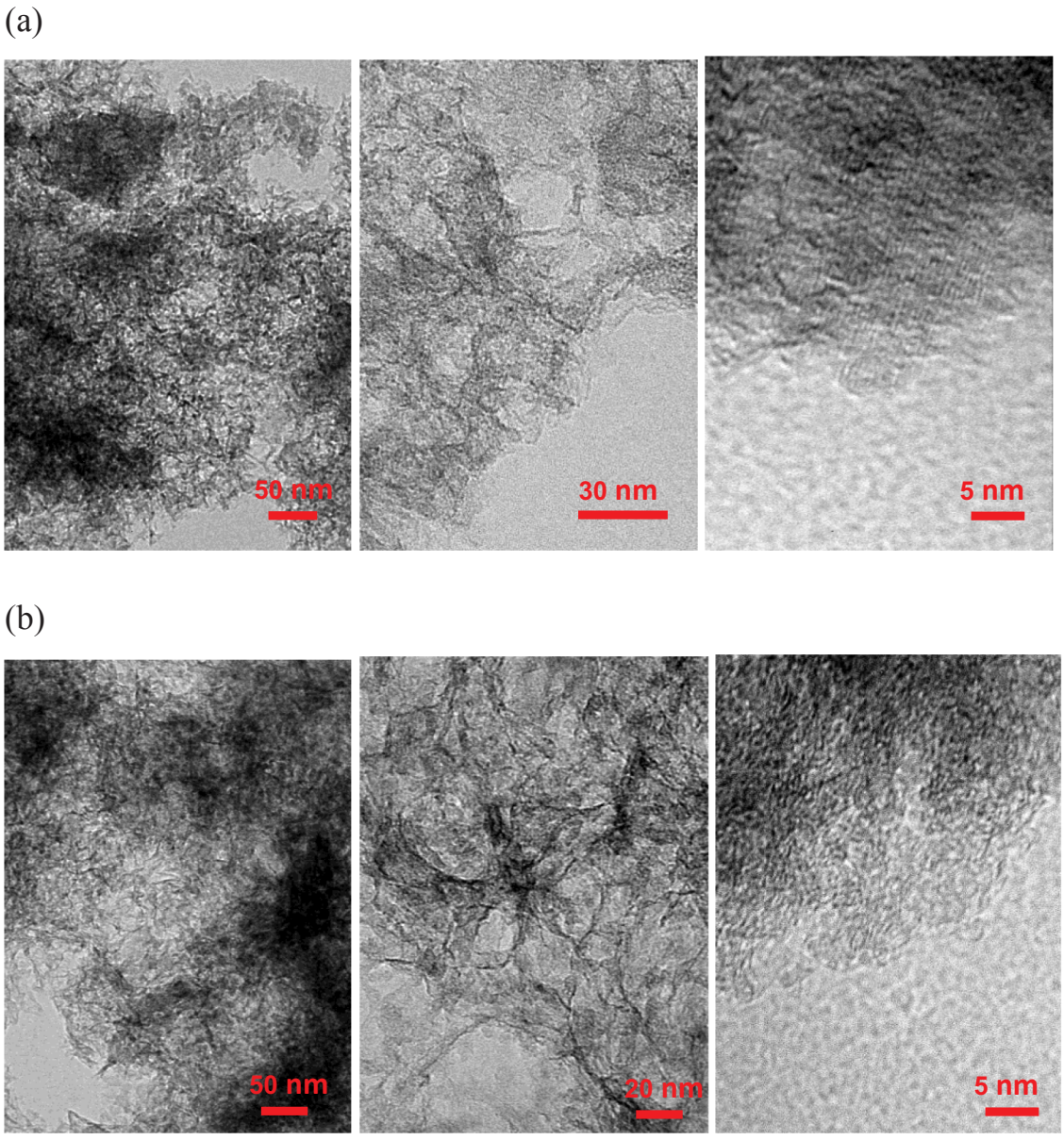


**Fig. 11.** Bright-field TEM pictures of samples treated with HF at two different magnifications: (a) SIOT45-HF; (b) SIOT104-HF.

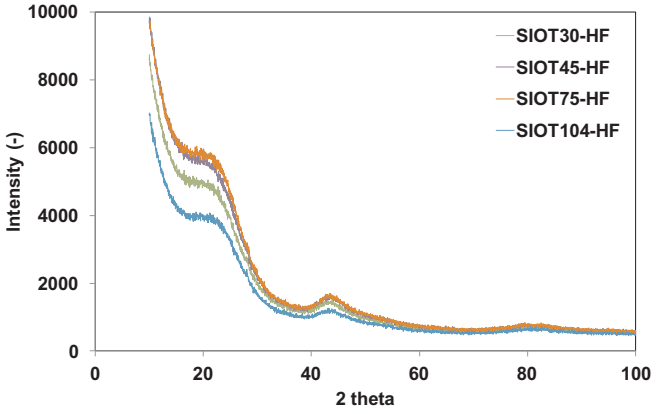


**Fig. 12.** XRD patterns of SIOT samples treated with HF.

**Table 3**
Structural parameters derived from the XRD data of Fig. 12.

| Sample | S/T mass ratio | Bragg angle 2θ (°) | Interlayer spacing $d_{002}$[a] (nm) | Crystallite size (nm) | | Average number of aromatic layers, $N_c$[c] |
|---|---|---|---|---|---|---|
| | | | | $L_a$[b] | $L_c$[b] | |
| SIOT30-HF | 0.30 | 23.22 | 0.38 | 2.59 | 1.19 | 3.12 |
| SIOT45-HF | 0.45 | 20.33 | 0.44 | 2.23 | 1.02 | 2.33 |
| SIOT75-HF | 0.75 | 22.71 | 0.39 | 2.10 | 0.96 | 2.47 |
| SIOT104-HF | 1.04 | 21.74 | 0.41 | 1.97 | 0.91 | 2.22 |

[a] Obtained from application of Bragg's law.
[b] Obtained from Eq. (6).
[c] Obtained from Eq. (7).

with $Na_2SiO_3$. The use of waterglass as a hardener is a great advantage as it was found to successfully replace the toxic and carcinogenic formaldehyde customarily employed for crosslinking tannin-based gels. Actually, $Na_2SiO_3$ plays a double role, firstly as a catalyst for auto-condensation of tannins, and secondly as a hard template able to drive the mesoporous structure of the final carbon aerogels. The present work has thus shown that autocondensation of tannin is a very effective route

to obtain carbon materials characterised by high surface area and presenting highly developed pore volumes, the latter being significantly higher than those of tannin-based carbon gels prepared in a classic way, e.g., by crosslinking with formaldehyde.

Furthermore, the pore texture parameters could be controlled by the silicate/tannin mass ratio. By applying different S/T ratios, the bulk density and hence the total porosity could be tuned. However, the BET area was hardly controlled by the initial amount of waterglass added to the formulation. On the other hand, it was observed that etching the silica that formed after pyrolysis of the organic gels with either NaOH or HF had a dramatic impact on the pore texture of the final carbon aerogels. It was found that the materials treated with HF were much more controllable than those obtained with NaOH. Carbons treated with HF presented clear trends of pore volumes as a function of S/T mass ratio and higher porosities than with NaOH, suggesting that treating those carbon gels with HF may result in well-developed and controlled porous properties.

Although practical applications have not been considered in the framework of the present paper, which was only devoted to the studies of synthesis mechanisms and of preparation – structure relationships, it is clear that the present carbon materials might be used as adsorbents in general, as catalyst supports, or as porous electrodes. In other words, all applications already reported and discussed for carbon aerogels (see for instance [67]) can be considered, and especially because these materials present even more developed porous structures than most of their counterparts. This will be the object of a forthcoming work.

## Acknowledgements

The authors gratefully acknowledge the financial support of the CPER 2007–2013 “Structuration du Pôle de Compétitivité Fibres Grand’Est (Competitiveness Fibre Cluster, France), through local (Conseil Général des Vosges), regional (Région Lorraine), national (DRRT and FNADT) and European (FEDER, France) funds.

## References

[1] S. Seyedsadr, R. Al Afif, C. Pfeifer, Hydrothermal carbonization of agricultural residues: a case study of the farm residues-based biogas plants, Carbon Resour. Convers. 1 (1) (2018) 81–85.
[2] G. Gao, L.Z. Cheong, D. Wang, C. Shen, Pyrolytic carbon derived from spent coffee grounds as anode for sodium-ion batteries, Carbon Resour. Convers. 1 (1) (2018) 104–108.
[3] J. Hou, Y. Ma, S. Li, W. Shang, A comparative study on characteristics of sulfur and nitrogen transformation and gaseous emission for combustion of bituminous coal and char, Carbon Resour. Convers. 1 (1) (2018) 86–93.
[4] A. Sharma, N. Sakimoto, T. Takanohashi, Effect of binder amount on the development of coal-binder interface and its relationship with the strength of the carbonized coal-binder composite, Carbon Resour. Convers. 1 (2) (2018) 139–146.
[5] Q. Wang, K. Li, Z. Guo, M. Fang, Z. Luo, K. Cen, Effects of $CO_2$ atmosphere on slow pyrolysis of high-ash lignite, Carbon Resour. Convers. 1 (1) (2018) 94–103.
[6] Z.D. Hood, S.P. Adhikari, S.F. Evans, H. Wang, Y. Li, A.K. Naskar, M. Chi, A. Lachgar, M. Parans Paranthaman, Tire-derived carbon for catalytic preparation of biofuels from feedstocks containing free fatty acids, Carbon Resour. Convers. 1 (3) (2018) 165–173.
[7] S. Ouyang, D. Xiong, Y. Li, L. Zou, J. Chen, Pyrolysis of scrap tyres pretreated by waste coal tar, Carbon Resour. Convers. 1 (3) (2018) 218–227.
[8] A. Pizzi, A Tannin-based adhesives, in: A. Pizzi (Ed.), Wood Adhesives: Chemistry and Technology, Marcel Dekker, New York, 1983, pp. 177–246.
[9] A. Pizzi, H. Pasch, A. Celzard, A. Szczurek, Oligomers distribution at the gel point of tannin-formaldehyde thermosetting wood adhesives, J. Adhes. Sci. Technol. 27 (2013) 2094–2102.
[10] G. Tondi, V. Fierro, A. Pizzi, A. Celzard, Tannin-based carbon foams, Carbon 47 (2009) 1480–1492.
[11] G. Tondi, W. Zhao, A. Pizzi, G. Du, V. Fierro, A. Celzard, Tannin-based rigid foams: a survey of chemical and physical properties, Bioresour. Technol. 100 (2009) 5162–5169.
[12] A. Szczurek, V. Fierro, A. Pizzi, M. Stauber, A. Celzard, A new method for preparing tannin-based foams, Ind. Crops Prod. 54 (2014) 40–53.
[13] G. Amaral-Labat, A. Szczurek, V. Fierro, A. Pizzi, A. Celzard, Systematic studies of tannin – formaldehyde aerogels: preparation and properties, Sci. Technol. Adv. Mater. 14 (015001) (2013) 13.
[14] G. Amaral-Labat, A. Szczurek, V. Fierro, N. Stein, C. Boulanger, A. Pizzi, A. Celzard, Pore structure and electrochemical performances of tannin-based carbon cryogels, Biomass Bioenergy 39 (2012) 274–282.
[15] G. Amaral-Labat, A. Szczurek, V. Fierro, A. Celzard, Unique bimodal carbon xerogels from soft templating of tannin, Mater. Chem. Phys. 149–150 (2015) 193–201.
[16] N. Rey-Raap, A. Szczurek, V. Fierro, A. Celzard, J. Angel Menéndez, A. Arenillas, Advances in tailoring the porosity of tannin-based carbon xerogels, Ind. Crops Prod. 82 (2016) 100–106.
[17] L.I. Grishechko, G. Amaral-Labat, V. Fierro, A. Szczurek, B.N. Kuznetsov, A. Celzard, Biosourced, highly porous, carbon xerogel microspheres, RSC Adv. 6 (2016) 65698–65708.
[18] F.L. Braghiroli, V. Fierro, M.T. Izquierdo, J. Parmentier, A. Pizzi, A. Celzard, Nitrogen-doped carbon materials produced from hydrothermally treated tannin, Carbon 50 (2012) 5411–5420.
[19] F.L. Braghiroli, V. Fierro, M.T. Izquierdo, J. Parmentier, A. Pizzi, C. Lacoste, L. Delmotte, A. Celzard, High surface – highly N-doped carbons from hydrothermally treatment of tannin, Ind. Crops Prod. 66 (2015) 282–290.
[20] F.L. Braghiroli, V. Fierro, A. Szczurek, N. Stein, J. Parmentier, A. Celzard, Hydrothermally treated aminated tannin as precursor of N-doped carbon gels for supercapacitors, Carbon 90 (2015) 63–74.
[21] S. Schlienger, A.L. Graff, A. Celzard, J. Parmentier, Direct synthesis of ordered mesoporous polymer and carbon materials by a biosourced precursor, Green Chem. 14 (2012) 313–316.
[22] F.L. Braghiroli, V. Fierro, J. Parmentier, A. Pasc, A. Celzard, Easy and eco-friendly synthesis of ordered mesoporous carbons by self-assembly of tannin with a block copolymer, Green Chem. 18 (2016) 3265–3271.
[23] A. Sanchez-Sanchez, M.T. Izquierdo, J. Ghanbaja, G. Medjahdi, S. Mathieu, A. Celzard, V. Fierro, Excellent electrochemical performances of nanocast ordered mesoporous carbons based on tannin-related polyphenols as supercapacitor electrodes, J. Power Sources 344 (2017) 15–24.
[24] A. Sanchez-Sanchez, M.T. Izquierdo, G. Medjahdi, J. Ghanbaja, A. Celzard, V. Fierro, Ordered mesoporous carbons obtained by soft-templating of tannin in mild conditions, Microporous Mesoporous Mater. 270 (2018) 127–139.
[25] A. Pizzi, K.L. Mittal, Handbook of Adhesive Technology, Revised and Expanded, CRC Press, 2003.
[26] S. Mulik, C. Sotiriou-Leventis, Resoprcinol-formaldehyde aerogels, in: M.A. Aegerter, N. Leventis, M.M. Koebel (Eds.), Aerogels Handbook, Springer, 2011, pp. 215–234.
[27] Lacoste, M.C. Basso, A. Pizzi, M.-P. Laborie, D. Garcia, A. Celzard, Bioresourced pine tannin/furanic foams with glyoxal and glutaraldehyde, Ind. Crops Prod. 45 (2013) 401–405.
[28] X. Li, A. Pizzi, X. Zhou, V. Fierro, A. Celzard, Formaldehyde-free prorobitenidin/profisetinidin tannin/furanic foams based on alternative aldehydes: glyoxal and glutaraldehyde, J. Renewable Mater. 3 (2015) 142–150.
[29] A. Szczurek, V. Fierro, A. Pizzi, A. Celzard, Mayonnaise, whipped cream and meringue, a new carbon cuisine, Carbon 58 (2013) 238–251.
[30] A. Szczurek, V. Fierro, A. Pizzi, A. Celzard, Emulsion-templated porous carbon monoliths derived from tannins, Carbon 74 (2014) 352–362.
[31] F. Braghiroli, V. Fierro, A. Pizzi, K. Rode, W. Radke, L. Delmotte, J. Parmentier, A. Celzard, Reaction of condensed tannins with ammonia, Ind. Crops Prod. 44 (2013) 330–335.
[32] J. Castro-Gutiérrez, A. Sanchez-Sanchez, J. Ghanbaja, N. Díez, M. Sevilla, A. Celzard, V. Fierro, Synthesis of perfectly ordered mesoporous carbons by liquid-assisted mechanochemical self-assembly of tannin, Green Chem. 20 (2018) 5123–5132.
[33] N. Meikleham, A. Pizzi, A. Stephanou, Induced accelerated autocondensation of polyflavonoid tannins for phenolic polycondensates. 1. $^{13}$C-NMR, $^{29}$Si-NMR, X-ray, and polarimetry studies and mechanism, J. Appl. Polymer Sci. 54 (1994) 1827–1845.
[34] A. Pizzi, N. Meikleham, Induced accelerated autocondensation of polyflavonoid tannins for phenolic polycondensates. III. CP-MAS 13C-NMR of different tannins and model, J. Appl. Polym. Sci. 55 (1995) 1265–1269.
[35] A. Merlin, A. Pizzi, An ESR study of the silica-induced autocondensation of polyflavonoid tannins, J. Appl. Polym. Sci. 59 (1996) 945–952.
[36] E. Masson, A. Merlin, A. Pizzi, Comparative kinetics of the induced radical autocondensation of polyflavonoid tannins, Part I: modified and non-modified tannins, J. Appl. Polymer Sci. 60 (1996) 263–269.
[37] E. Masson, A. Pizzi, A. Merlin, Comparative kinetics of the induced radical autocondensation of polyflavonoid tannins – Part 2: flavonoid units effects, J. Appl. Polym. Sci. 64 (1997) 243–265.
[38] R. Garcia, A. Pizzi, A. Merlin, Ionic polycondensation effects on the radical autocondensation of polyflavonoid tannins – an ESR study, J. Appl. Polym. Sci. 65 (1997) 2623–2632.
[39] A. Pizzi, N. Meikleham, B. Dombo, W. Roll, Autocondensation-based, zero-emission, tannin adhesives for particleboard, Holz als Roh- und Werkstoff 53 (1995) 201–204.
[40] R. Garcia, A. Pizzi, Polycondensation and autocondensation networks in polyflavonoid tannins, Part 1: final networks, J. Appl. Polym. Sci. 70 (1998) 1083–1091.
[41] R. Garcia, A. Pizzi, Polycondensation and autocondensation networks in polyflavonoid tannins, Part 2: polycondensation vs. autocondensation, J. Appl. Polym. Sci. 70 (1998) 1093–1110.
[42] S. Brunauer, P.H. Emmet, E. Teller, Adsorption of gases in multimolecular layers, J. Am. Chem. Soc. 60 (2) (1938) 309–319.
[43] M.M. Dubinin, Fundamentals of the theory of adsorption in micropores of carbon adsorbents: characteristics of their adsorption properties and microporous structures, Carbon 27 (1989) 457–567.
[44] S.J. Gregg, K.S.W. Sing, Adsorption, Surface Area and Porosity, second ed., Academic Press, London, 1982.
[45] F. Stoeckli, A. Slasli, D. Hugi-Cleary, A. Guillot, The characterization of

microporosity in carbons with molecular sieve effects, Microporous Mesoporous Mater. 51 (3) (2002) 197–202.
[46] M.M. Dubinin, Generalization of the theory of volume filling of micropores to nonhomogeneous microporous structures, Carbon 23 (1985) 373–380.
[47] J. Jagiello, J.P. Olivier, 2D-NLDFT adsorption models for carbon slit-shaped pores with surface energetical heterogeneity and geometrical corrugation, Carbon 55 (2013) 70–80.
[48] T.A. Centeno, F. Stoeckli, The assessment of surface areas in porous carbons by two model-independent techniques, the DR equation and DFT, Carbon 48 (9) (2010) 2478–2486.
[49] E.P. Barret, L.G. Joyner, P.P. Halenda, The determination of pore volume and area distributions in porous substances. I. Computations from nitrogen isotherms, J. Am. Chem. Soc. 73 (1951) 373–380.
[50] M. Kruk, M. Jaroniec, M. Sayari, Application of large pore MCM-41 molecular sieves to improve pore size analysis using nitrogen adsorption measurements, Langmuir 13 (1997) 6267–6273.
[51] H. Takagi, K. Maruyama, N. Yoshizawa, Y. Yamada, Y. Sato, XRD analysis of carbon stacking structure in coal during heat treatment, Fuel 83 (2004) 2427–2433.
[52] S. Bernard, O. Beyssac, K. Benzerara, N. Findling, G. Tzvetkov, G.E. Brown Jr., XANES, Raman and XRD study of anthracene-based cokes and saccharose-based chars submitted to high-temperature pyrolysis, Carbon 48 (2010) 2506–2516.
[53] V. Fierro, A. Sanchez-Sanchez, A. Celzard, Chapter 13: Tannins as precursors of supercapacitor electrodes, CRC Press, Taylor & Francis, 2017, pp. 201–228.
[54] W. Zhao, V. Fierro, A. Pizzi, A. Celzard, Bimodal cellular activated carbons derived from tannins, J. Mater. Sci. 45 (2010) 5778–5785.
[55] A. Szczurek, G. Amaral-Labat, V. Fierro, A. Pizzi, E. Masson, A. Celzard, The use of tannin for preparing carbon gels. Part I. Carbon aerogels, Carbon 49 (2011) 2773–2784.
[56] A. Szczurek, G. Amaral-Labat, V. Fierro, A. Pizzi, A. Celzard, The use of tannin to prepare carbon gels, Part II: Carbon Cryogels, Carbon 49 (2011) 2785–2794.
[57] A. Szczurek, V. Fierro, A. Pizzi, M. Stauber, A. Celzard, Carbon meringues derived from flavonoid tannins, Carbon 65 (2013) 214–227.
[58] F.L. Braghiroli, V. Fierro, J. Parmentier, L. Vidal, P. Gadonneix, A. Celzard, Hydrothermal carbons produced from tannin by modification of the reaction medium: addition of $H^{\pm}$ and $Ag^{\pm}$, Ind. Crops Prod. 77 (2015) 364–374.
[59] F.L. Braghiroli, V. Fierro, A. Szczurek, P. Gadonneix, J. Ghanbaja, J. Parmentier, G. Medjahdi, A. Celzard, Hydrothermal treatment of tannin: a route to porous metal oxides and metal/carbon hybrid materials, Inorganics 5 (2017) 7-1–7-19.
[60] A. Sánchez-Sánchez, M.T. Izquierdo, S. Mathieu, J. González-Álvarez, A. Celzard, V. Fierro, Outstanding electrochemical performances of highly N- and O-doped carbons derived from pine tannin, Green Chem. 19 (2017) 2653–2665.
[61] F.L. Braghiroli, V. Fierro, M.T. Izquierdo, J. Parmentier, A. Pizzi, A. Celzard, Kinetics of the hydrothermal treatment of tannin for producing carbonaceous microspheres, Bioresour. Technol. 151 (2014) 271–277.
[62] A. Celzard, V. Fierro, G. Amaral-Labat, A. Szczurek, F. Braghiroli, J. Parmentier, A. Pizzi, L.I. Grishechko, B.N. Kuznetsov, Carbon gels derived from natural resources (Geles de carbón de origen natural), Boletín del Grupo Español del Carbón (2012) 2–7.
[63] M. Thommes, K. Kaneko, A.V. Neimark, J.P. Olivier, F. Rodriguez-Reinoso, J. Rouquerol, K.S.W. Sing, Physisorption of gases, with special reference to the evaluation of surface area and pore size distribution (IUPAC Technical Report), Pure Appl. Chem. 87 (9–10) (2015) 1051–1069.
[64] K. Meyer, K.P. Klobes, Comparison between different presentations of pore size distribution in porous materials, Fresenius J. Anal. Chem. 363 (1999) 174–178.
[65] G.T. Adylov, Sh.A. Faiziev, M.S. Paizullakhanov, S. Mukhsimov, É. Nodirmatov, Silicon carbide materials obtained from rice husk, Tech. Phys. Lett. 29 (3) (2003) 221–223.
[66] S. Schaefer, V. Fierro, G. Muñiz, M.T. Izquierdo, S. Mathieu, M.L. Ballinas-Casarrubias, G. González-Sánchez, A. Celzard, Rice straw-based activated carbons doped with SiC for enhanced hydrogen adsorption, Int. J. Hydrogen Energy 42 (2017) 11534–11540.
[67] A. Celzard, V. Fierro, G. Amaral-Labat, Adsorption by carbon gels, in: J.D. Tascon (Ed.), Novel Carbon Adsorbents, Elsevier, 2012, pp. 207–244.